Available on the CERN CDS information server **CMS PAS HIG-11-012**

CMS Physics Analysis Summary

Contact: cms-pag-conveners-higgs@cern.ch 2011/08/28

Search for the Standard Model Higgs Boson Decaying to Bottom Quarks and Produced in Association with a W or a Z Boson

The CMS Collaboration

Abstract

A search for the standard model Higgs boson is performed in a data sample corresponding to an integrated luminosity of 1.1 fb^{-1}, recorded by the CMS detector in proton-proton collisions at the LHC with a 7 TeV center-of-mass energy. The following modes are studied: $W(\mu\nu)H$, $W(e\nu)H$, $Z(\mu\mu)H$, $Z(ee)H$ and $Z(\nu\nu)H$, with the Higgs decaying to $b\bar{b}$ pairs. 95% C.L. upper limits on the VH production cross section are derived for a Higgs mass between 110 and 135 GeV. The expected (observed) upper limit at 115 GeV is found to be 5.7 (8.3) times the standard model expectation.

1 Introduction

The process by which the electroweak symmetry is broken in Nature remains elusive. In the standard model (SM) the Higgs mechanism [1–3] is considered as the most likely explanation. The search for the Higgs boson is currently one of the most important undertakings of experimental particle physics.

Measurements of the W and top-quark masses at LEP and the Tevatron, combined with precision measurements of electroweak parameters at the Z pole, provide an indirect constraint on the Higgs mass of $m_H < 158\,\text{GeV}$ at 95% confidence level (C.L.) [4]. Previous direct searches at the LEP experiments set a lower bound of $m_H > 114.4\,\text{GeV}$ at 95% C.L. [5], while direct searches at the Tevatron currently exclude the region 156–177 GeV [6], also at 95% C.L.

Preliminary search results from CMS [7–12] and ATLAS [13] are excluding even higher masses, and are starting to broaden the exclusion region near 165 GeV. The most likely mass for the SM Higgs is therefore at "low mass" near the LEP limit, where the Higgs decays predominantly into $b\bar{b}$ pairs.

At the LHC the main Higgs production mechanism is direct production through gluon fusion, with a cross section of $\sim 17 \cdot 10^3$ fb for a Higgs mass $m_H = 120$ GeV [14–29]. However, in this production mode, the detection of the $H \to b\bar{b}$ decay is rendered nearly impossible due to overwhelming QCD di-jet production. The same holds true for the next most copious production mode, through vector-boson fusion, with a cross section of $\sim 1,300$ fb. Processes in which the Higgs is produced in association with a vector boson have cross sections of ~ 660 and ~ 360 fb for WH and ZH respectively. Until now these VH processes, with $H \to b\bar{b}$, have not been considered as promising, in terms of sensitivity, as the relatively more clean, but heavily suppressed, final states: $H \to \gamma\gamma$ and $H \to \tau\tau$. Even if this is the case, it is paramount to search for the Higgs in these modes given that the observation of the $H \to b\bar{b}$ decay is key to determine the nature of this particle, if and when discovered.

In this note a summary of a search for the standard model Higgs boson in the $pp \to VH$ production mode is presented. The analysis is performed in a data sample corresponding to an integrated luminosity of 1.1 fb^{-1}, collected by the CMS experiment at a 7 TeV center-of-mass energy. The following final states are included: $W(\mu\nu)H$, $W(e\nu)H$, $Z(\mu\mu)H$, $Z(ee)H$ and $Z(\nu\nu)H$ –all with the Higgs decaying to $b\bar{b}$ pairs.

Backgrounds arise from production of W and Z bosons associated with jets (all flavors), singly and pair-produced top quarks, and di-bosons. Simulated samples of all backgrounds are used to provide guidance in the analysis optimization, and an initial evaluation of their contributions in the search region. For the main backgrounds, high-purity control regions are used to estimate their contribution in the signal region.

An optimization of the event selection, that depends on the Higgs mass, is performed, and 95% C.L. upper limits on the $pp \to VH$ production cross section are obtained for Higgs masses between 110-135 GeV. These limits are based on the observed event count and background estimate in signal regions defined in either the invariant mass distribution of $H \to b\bar{b}$ candidates ("$M(\text{jj})$ or cut-and-count analysis"), or in the output discriminant of a boosted decision tree algorithm ("`BDT` analysis"). The latter enhances the statistical power of the analysis by making full use of correlations between discriminating variables in signal and background events.

2 The CMS Detector and Simulated Samples

A detailed description of the CMS detector can be found elsewhere [30]. The key components of the detector include a silicon pixel and a silicon strip tracker, immersed in a 3.8 T solenoidal magnetic field, which are used to measure the momenta of charged particles. The tracker, which covers the pseudorapidity range $|\eta| < 2.5$, is surrounded by a crystal electromagnetic calorimeter (ECAL) and a brass-scintillator hadronic calorimeter (HCAL). The ECAL and HCAL extend to a pseudorapidity range of $|\eta| < 3.0$. A quartz fiber Cherenkov forward detector (HF) extends the calorimetric coverage to $|\eta| < 5.0$. The outermost component of the CMS detector is the muon system consisting of gas detectors placed in the iron return yoke to measure the momentum of muons traversing through the detector.

Simulated samples of signal and backgrounds were produced using various event generators, with the CMS detector response modeled in extensive detail with `GEANT4` [31]. The Higgs signal samples were produced using `POWHEG` [32] interfaced with the `HERWIG` [33] parton shower generator. The diboson samples come from `Pythia6` [34] and `MadGraph` [35] is used for W+jets and Z+jets. For $t\bar{t}$ production the simulated samples were produced using `MadGraph`. The single-top samples were produced with `POWHEG` and the QCD samples with `Pythia`. All samples were generated with a roughly flat pileup (PU) distribution up to 10 interactions per proton bunch crossings. The PU interactions are overlapping minimum-bias events added at random within the proton-proton interaction region. During the period in which the data for this analysis was recorded the LHC instantaneous luminosity reached up to $\sim 1.4 \cdot e^{33} cm^{-2} s^{-1}$ and the average number of interactions per bunch crossing was about six. The simulated samples were reweighted to represent the PU distribution measured in the data.

3 Trigger and Event Reconstruction

Several triggers were used to collect events consistent with the signal hypothesis in all five channels.

For the WH channels the trigger paths require single-lepton triggers with tight lepton identification, calorimeter and tracker isolation requirements applied to maintain an acceptable trigger rate. For the W($\mu\nu$)H channel the p_T threshold for the muon trigger was 17 GeV. This trigger was used for the complete dataset and was 70-95% efficient, depending on rapidity and p_T . Its effective efficiency for muons from signal, reconstructed offline with $p_T > 20$ GeV, was $\sim$ 90%. For the W($e\nu$)H channel the trigger for the first 200 pb^{-1} of data required a single electron with $E_T > 27$ GeV. The effective efficiency was $\sim$ 95% for electrons reconstructed offline with $E_T > 30$ GeV. For the next $\sim$ 300 pb^{-1} the single electron trigger threshold was reduced to 17 GeV by adding the requirement of two jets and pfMHT -which is the resulting missing transverse energy (E_T^{miss}) when adding up the transverse energy of all jets reconstructed with a particle flow algorithm [36]. The jets E_T thresholds were 30 and 25 GeV for the leading and sub-leading jet, respectively. The pfMHT threshold was 15 GeV. For the last $\sim$ 600 pb^{-1} the electron and pfMHT thresholds were raised to 22 and 30 GeV, respectively. The effective efficiency for these triggers for signal events that pass the final offline selection criteria in Section 4 was $\sim$97%.

For the Z($\mu\mu$)H channel the same single muon trigger, described above, was used; while for the Z(ee)H channel, a di-electron trigger with lower E_T thresholds 17/8 GeV and very tight isolation requirements was used. Both of these triggers were $\sim$ 99% efficient for the 20/20 GeV p_T (E_T) offline threshold combination used on both muons (electrons).

For the Z($\nu\nu$)H channel, combinations of three triggers were used. The first one required

pfMHT$>$ 150 GeV and was used for the complete dataset. The second and third one allow a lower $E_{\mathrm{T}}^{\mathrm{miss}}$ threshold of 80 GeV (reconstructed from all energy deposits in the calorimeter). For the second one the presence of a central jet ($|\eta| < 2.4$) above a E_{T} threshold of 80 GeV was required, and for the third trigger the requirement was that there be two central jets with E_{T} > 20 GeV. For the first ~ 200 pb^{-1} of data events were required to pass the OR of the first two triggers and for the last ~ 900 pb^{-1} the requirement was that they pass the OR of the first and third trigger. The effective trigger efficiency was 50% for an offline pfMET of 120 GeV and $\sim$ 98% above the 160 GeV threshold used for the offline event selection. The relatively high $E_{\mathrm{T}}^{\mathrm{miss}}$ thresholds were needed to keep the trigger rate under control.

The reconstructed interaction vertex with the largest value of $\sum_i p_{\mathrm{T}i}^2$, amongst all reconstructed vertices, is selected as the primary event vertex ($p_{\mathrm{T}i}$ is the transverse momentum of the i-th track in the vertex). The primary vertex is used as reference for all other objects reconstructed in the event.

All relevant objects in the event are reconstructed offline with the particle-flow algorithm. The extra PU interactions affect jet momentum reconstruction, $E_{\mathrm{T}}^{\mathrm{miss}}$ reconstruction, lepton isolation and b-tagging efficiency. To mitigate these effects a track-based algorithm that filters all charged hadrons that do not appear to originate from the primary interaction is used. In addition a calorimeter-based algorithm evaluates the energy density in the calorimeter from interactions not related to the primary vertex and subtracts it from reconstructed jets in the event.

Jets are defined as particle-flow objects clustered with the anti-k_{T} algorithm [37] using a size parameter of 0.5. Each jet is required to lie within $|\eta| < 2.5$, have at least two tracks associated to it, and have electromagnetic and hadronic energy fractions of at least 1% of the total energy. Standard jet-energy corrections are applied [38].

The $\vec{E}_{\mathrm{T}}^{\mathrm{miss}}$ vector is calculated as the negative of the vectorial sum of transverse momenta of all particle-flow objects identified in the event, and the magnitude of this vector is referred to as pfMET. This value divided by the square root of the scalar sum of E_{T} of all particle-flow objects is referred to as the "pfMET significance".

Electron reconstruction involves matching particle-flow objetcs: energy clusters in the ECAL with tracks in the silicon tracker [39]. Identification criteria based on the ECAL shower shape, track-ECAL cluster matching and consistency with the primary vertex are imposed. Electron candidates that fall in the transition region between ECAL barrel and endcap ($1.442 < |\eta| < 1.566$) are rejected. Additional requirements are imposed to remove electrons produced by photon conversions. In this analysis electrons are considered in the pseudorapidity range $|\eta| < 2.5$, excluding the gap region $1.44 < |\eta| < 1.57$. In addition an isolation requirement is applied; the sum of calorimeter energy and track momenta in a cone of radius 0.4 around the electron is computed and electrons are rejected if this sum is larger than 10% of the electron momentum. The electron reconstruction efficiency is close to 100%.

Muons are reconstructed using two algorithms - one in which tracks in the silicon tracker are matched to hits in the muon chamber and another in which a global track fit is performed seeded by hits in the muon system [40]. The muon candidates used in the analysis are required to be reconstructed successfully with both algorithms. Further identification criteria based on the number of hits in the tracker and the muon system, the fit quality of the muon track and its consistency with the primary vertex, are imposed on the muon candidates to reduce fakes. The muon reconstruction efficiency is also close to 100%.

The CSV ("Combined Seconday Vertex") b-tagging algorithm [41, 42] is used to identify jets that are likely to arise from the fragmentation and hadronization of b quarks. This algorithm

combines in an optimal way the information about track impact parameters and secondary vertices within jets in a likelihood discriminant to provide maximal separation of b-jets from jets originating from light quarks and gluons, and also from charm quarks. The CSV output discriminant is continous and different optimal working points can be selected.

All events from data and from the simulated samples are required to pass the same trigger and event reconstruction algorithms. Scale factors to account for the differences in the performance of these algorithms between data and simulations are computed and used in the analysis.

4 Event Selection

The main backgrounds to VH production include vector-boson plus heavy (W/Z+bb) and light (W/Z+udscg) jets, $t\bar{t}$, single-top (ST), di-bosons (VV) and QCD. These overwhelm the VH signal by several orders of magnitude. The signal event selection is therefore tight and it aims to reconstruct kinematically the W/Z vector bosons and the Higgs decay into two b-jets, while also reducing the background significantly. The event selection was optimized for significance, taking into account available statistics (in the signal and control regions) and the possible sculpting of the $M(\mathrm{jj})$ distribution. We first describe the selection used to count events in the $M(\mathrm{jj})$ analysis, and then the selection used to count events in the BDT analysis. The final event selection for each of the five channels considered was optimized separately.

4.1 Selection for the $M(\mathrm{jj})$ Analysis

Candidate $W \to \ell\nu$ decays are identified by requiring the presence of a single, isolated, lepton and additional missing transverse energy. Muons (electrons) are required to have a p_T above 20 (30) GeV. Candidate $Z \to \ell\ell$ decays are reconstructed by combining isolated, opposite charge pairs of electrons and muons and requiring the dilepton invariant mass to satisfy $75 < m_{\ell\ell} < 105\,\mathrm{GeV}$. For Z candidates the electron p_T is lowered to 20 GeV. The identification of $Z \to \nu\bar{\nu}$ decays requires pfMET $> 160\,\mathrm{GeV}$ (the high threshold dictated by the trigger).

The reconstruction of the $H \to b\bar{b}$ decay is made by requiring the presence of two central ($|\eta| < 2.5$) particle-flow jets, above a minimum p_T threshold and tagged by the CSV algorithm. If more than two such jets are found in the event, the pair with the highest sum of the CSV outputs for the two jets is chosen (except for the WH analyses, in which the $t\bar{t}$ background is larger, where the pair of jets with highest total p_T is chosen). These combinations are found to yield higher efficiency and rejection of wrong combinations in signal events, as opposed to simply selecting the two highest p_T jets in the event. After b-tagging the fraction of $H \to b\bar{b}$ candidates that contain the two b-jets from the Higgs decay is near unity. For the tight CSV cut value (> 0.898) used for b-tagging (see Table 1) the efficiencies to tag b-quarks, c-quarks and light quarks were approximately 50%, 6% and 0.15%. The corresponding efficiencies for the looser CSV cut (> 0.5) were approximately 72%, 23% and 3%.

After b-tagging, the background from V+jets and di-bosons is reduced significantly and becomes dominated by the sub-processes where the two jets originate from real b-quarks. Events with additional jets (N_{aj}) or additional leptons (N_{al}) are rejected to further reduce backgrounds from $t\bar{t}$ and WZ.

The topology of VH production is such that the W/Z and the Higgs recoil away from each other with significant p_T. Cuts on the azimuthal opening angle between the vector boson and the reconstructed momenta of the Higgs candidate, $\Delta\phi(V, H)$, on the p_T of the V-boson and on the b-tagged dijet pair achieve significant rejection for most background processes and improve the analysis reach.

Table 1: Final selection applied to each channel in the $M(\mathrm{jj})$ analyses, including the sliding windows on $M(\mathrm{jj})$ for each mass point. Entries marked "–" indicate that there is no cut applied to the given variable in that channel. The first two lines refer to the p_{T} threshold on the leading (b_1) and sub-leading (b_2) Higgs daughters, while CSV1 (CSV2) are the max (min) b-tags for the two jets.

Variable	$\mathrm{W}(\ell\nu)\mathrm{H}$	$\mathrm{Z}(\ell\ell)\mathrm{H}$	$\mathrm{Z}(\nu\nu)\mathrm{H}$
$\mathrm{m}_{\ell\ell}$	–	$75 < \mathrm{m}_{\ell\ell} < 105$	–
$p_{\mathrm{T}}(b_1)$	> 30	> 20	> 80
$p_{\mathrm{T}}(b_2)$	> 30	> 20	> 30
$p_{\mathrm{T}}(\mathrm{jj})$	> 165	> 100	> 160
$p_{\mathrm{T}}(\mathrm{V})$	> 160	> 100	–
CSV1	> 0.898	> 0.898	> 0.898
CSV2	> 0.5	> 0.5	> 0.5
$\Delta\phi(\mathrm{V},\mathrm{H})$	> 2.95	> 2.90	> 2.90
N_{aj}	$= 0$	< 2	–
N_{al}	$= 0$	–	$= 0$
pfMET	$> 35(\mathrm{W}(\mathrm{e}\nu)\mathrm{H})$	–	> 160
pfMETsig	–	–	> 5
$\Delta\phi(\mathrm{pfMET},\mathrm{J})$	–	–	> 1.5
$M(\mathrm{jj})(110)$	95–125	90–120	95–125
$M(\mathrm{jj})(115)$	100–130	95–125	100–130
$M(\mathrm{jj})(120)$	105–135	100–130	105–135
$M(\mathrm{jj})(125)$	110–140	105–135	110–140
$M(\mathrm{jj})(130)$	115–145	110–140	115–145
$M(\mathrm{jj})(135)$	120–150	115–145	120–150

For the $\mathrm{Z} \to \nu\bar{\nu}$ channel, QCD backgrounds are further reduced by a factor of ~ 30 when requiring that the pfMET does not originate from mismeasured jets. A cut on the azimuthal angle between the pfMET and the closest jet, $\Delta\phi(\mathrm{pfMET},\mathrm{J}) > 1.5$, is applied, together with the requirement that pfMET significance be > 5.

Table 1 summarizes the selection criteria used in each of the five channels. Table 2 summarizes the signal efficiency of the selection criteria for the $M(\mathrm{jj})$ analysis applied to each channel. All criteria are applied except for the trigger selection, which is measured separately. In addition, data/MC scale factors have been determined for lepton reconstruction and identification efficiencies, as well as the efficiency of tagging b-jets.

4.2 BDT Selection

The `BDT` analysis is implemented in the TMVA framework [43]. The training is done with simulated samples for signal and background that pass a looser event selection relative to the $M(\mathrm{jj})$ analyses. Table 3 summarizes the final selection of the `BDT` analyses. Several input variables were chosen by iterative optimization. These include the di-jet invariant mass and momentum: $M(\mathrm{jj})$ and $p_{\mathrm{T}}(\mathrm{jj})$, the V transverse momentum $p_{\mathrm{T}}(\mathrm{V})$, the CSV value for each of the two jets, the azimuthal angle between the V and the dijets, $\Delta\phi(\mathrm{V},\mathrm{H})$, and the pseudorapidity separation between the two jets, $\Delta\eta(\mathrm{J1},\mathrm{J2})$. The `BDT` analysis was expected to improve the sensitivity with respect to the $M(\mathrm{jj})$ analysis by about 10% in every channel.

Table 2: Signal efficiencies (%) for the $M(\mathrm{jj})$ analysis selection in each channel as determined in the POWHEG signal Monte Carlo samples for $M_{\mathrm{H}} = 115\,\mathrm{GeV}$. Each sample includes 220000 events produced. "Pre-select" includes all criteria described in the text used to select the W/V/H bosons, other than those listed in this Table. Entries marked with "–" indicate that the variable is not used in the selection for that channel. The efficiency of each criterion is relative to the ones above. Uncertainties are statistical only.

Pre-select	13.40 ± 0.07	9.67 ± 0.06	12.88 ± 0.07	10.76 ± 0.07	20.02 ± 0.09
$p_{\mathrm{T}}(\mathrm{jj})$	11.70 ± 0.19	14.00 ± 0.24	28.50 ± 0.27	29.26 ± 0.30	23.51 ± 0.20
$p_{\mathrm{T}}(\mathrm{V})$	75.50 ± 0.73	78.29 ± 0.76	85.31 ± 0.39	85.65 ± 0.42	–
CSV1	64.13 ± 0.94	62.58 ± 1.00	68.02 ± 0.56	68.46 ± 0.60	67.01 ± 0.46
CSV2	55.75 ± 1.22	54.45 ± 1.30	59.17 ± 0.72	58.73 ± 0.77	63.51 ± 0.58
$\Delta\phi(\mathrm{V,H})$	86.90 ± 1.11	90.44 ± 1.04	83.51 ± 0.70	83.57 ± 0.76	78.35 ± 0.62
N_{aj}	74.78 ± 1.53	72.46 ± 1.67	92.57 ± 0.55	93.18 ± 0.56	–
N_{al}	100	100	–	–	99.88 ± 0.06
pfMET	–	88.34 ± 1.43	–	–	76.31 ± 0.72
pfMETsig	–	–	–	–	99.92 ± 0.05
$\Delta\phi(\mathrm{pfMET,J})$	–	–	–	–	79.00 ± 0.79
$M(\mathrm{jj})$	80.17 ± 1.62	81.38 ± 1.71	73.54 ± 0.95	73.20 ± 1.03	72.70 ± 0.98
Total Eff.	0.22 ± 0.01	0.17 ± 0.01	0.72 ± 0.02	0.62 ± 0.02	0.69 ± 0.02

Table 3: Training selection and final signal region in each channel in the BDT analyses. Entries marked "–" indicate that the variable is not used in the given channel. For $\mathrm{Z}(\nu\nu)\mathrm{H}$ and $\mathrm{Z}(\mu\mu)\mathrm{H}$ the signal window lower boundary was optimized separately for each mass point (from 110 to 135): For $\mathrm{Z}(\nu\nu)\mathrm{H}$ the values are: -0.160, -0.175, -0.215, -0.175, -0.185, -0.215, and the corresponding $\mathrm{Z}(\mu\mu)\mathrm{H}$ values are: -0.198, -0.147, -0.147, -0.198, -0.147, -0.198.

Variable	$\mathrm{W}(\mu\nu)\mathrm{H}$	$\mathrm{W}(\mathrm{e}\nu)\mathrm{H}$	$\mathrm{Z}(\mu\mu)\mathrm{H}$	$\mathrm{Z}(\mathrm{ee})\mathrm{H}$	$\mathrm{Z}(\nu\nu)\mathrm{H}$
$\mathrm{m}_{\ell\ell}$	–	–	$75 < \mathrm{m}_{\ell\ell} < 105$	$75 < \mathrm{m}_{\ell\ell} < 105$	–
$p_{\mathrm{T}}(b_1)$	> 30	> 30	> 20	> 20	> 80
$p_{\mathrm{T}}(b_2)$	> 30	> 30	> 20	> 20	> 20
$p_{\mathrm{T}}(\mathrm{jj})$	> 150	> 150	–	–	> 160
$p_{\mathrm{T}}(\mathrm{V})$	> 150	> 150	–	–	–
CSV1	> 0.40	> 0.40	> 0.24	> 0.24	> 0.50
CSV2	> 0.40	> 0.40	> 0.24	> 0.24	> 0.50
N_{aj}	–	–	< 2	< 2	–
N_{al}	$= 0$	$= 0$	–	–	$= 0$
$\Delta\phi(\mathrm{pfMET,J})$	–	–	–	–	> 0.5
pfMETsig	–	> 2	–	–	> 5
BDT	> 0.050	> 0.040	variable	> 0.160	variable

Table 4: Purity and scale factors (Data/MC) derived from background enriched control regions, as described in the text. The scale factors for W($\mu\nu$)H and W(eν)H were averaged together, and the same was done for Z($\mu\mu$)H and Z(ee)H.

Control region	W($\mu\nu$)H Purity	W(eν)H Purity	W($\ell\nu$)H SF	Z($\mu\mu$)H Purity	Z(ee)H Purity	Z($\ell\ell$)H SF
V + udscg	80.2%	79.4%	0.84 ± 0.10	92.8%	95.4%	0.88 ± 0.02
$t\bar{t}$	85.6%	85.8%	1.01 ± 0.11	95.4%	97.5%	0.99 ± 0.05
V+$b\bar{b}$	20.1%	20.2%	1.40 ± 0.29	83.7%	81.6%	1.16 ± 0.08

5 Background Control Regions

Appropriate control regions that are orthogonal to the signal region are identified in data and used to adjust Monte Carlo estimates for the most important background processes: W + jets and Z + jets (with light and heavy-flavor jets), $t\bar{t}$ and QCD multijet and heavy-quark production. Different control regions are found for each of the different search channels by changing the event selection in a way that enriches the content of each specific background. For all cases, control regions with purity ranging from about 20% to nearly 100% have been successfully found. Discrepancies between the expected and observed yields in the data in these control regions are used to obtain a scale factor by which the estimates from the simulation are adjusted. The background from these sources in the signal region are then estimated from the adjusted simulation samples, taking into account the associated systematic uncertainty. The precise construction of all the control regions is involved and outside the scope of this summary note. The procedures applied include, for example: reversing the b-tagging requirements to enhance W + jets and Z + jets with light-flavor jets; enforcing a tighter b-tag requirement and requiring extra jets to enhance $t\bar{t}$ and requiring low "boost" in order to enhance V$b\bar{b}$ over $t\bar{t}$. Table 4 lists the control regions and the corresponding purities and scale factors obtained. Figure 1 shows some examples of these control regions for the W($\ell\nu$)H and the Z($\ell\ell$)H analyses.

The Z($\nu\nu$)H channel is unique among the five modes analyzed, in that it does not include charged leptons. An important check is to compare the observed pfMET distribution with the predicted distribution from simulation. To accomplish this, muons are removed from the Z($\mu\mu$)+jets data sample. In Fig. 2, the resulting pfMET distribution is compared to Z($\nu\nu$)H simulated events. Good overall agreement is found. Reasonably pure samples of $t\bar{t}$ and W + jets events can be obtained by requiring at least one additional isolated lepton in the event, and then either requiring (for $t\bar{t}$) or vetoing (for W + jets) b-jets. Table 5 lists the control regions and the corresponding purities and scale factors obtained. Some of the corresponding distributions are shown in Fig. 2.

The QCD background in the signal region is also estimated from data using control regions of high and low values of two uncorrelated variables with significant discriminating power towards QCD events. One is the angle between the missing energy vector and the closest jet in azimuth, $\Delta\phi(\text{pfMET}, \text{J})$ and the other is the sum of the CSV values of the two b-tagged jets. The signal region is at high values of both discriminants, while QCD populates regions with low values of either. The method predicts a very small contamination of 0.015 ± 0.008 QCD background events, which we consider to be negligible.

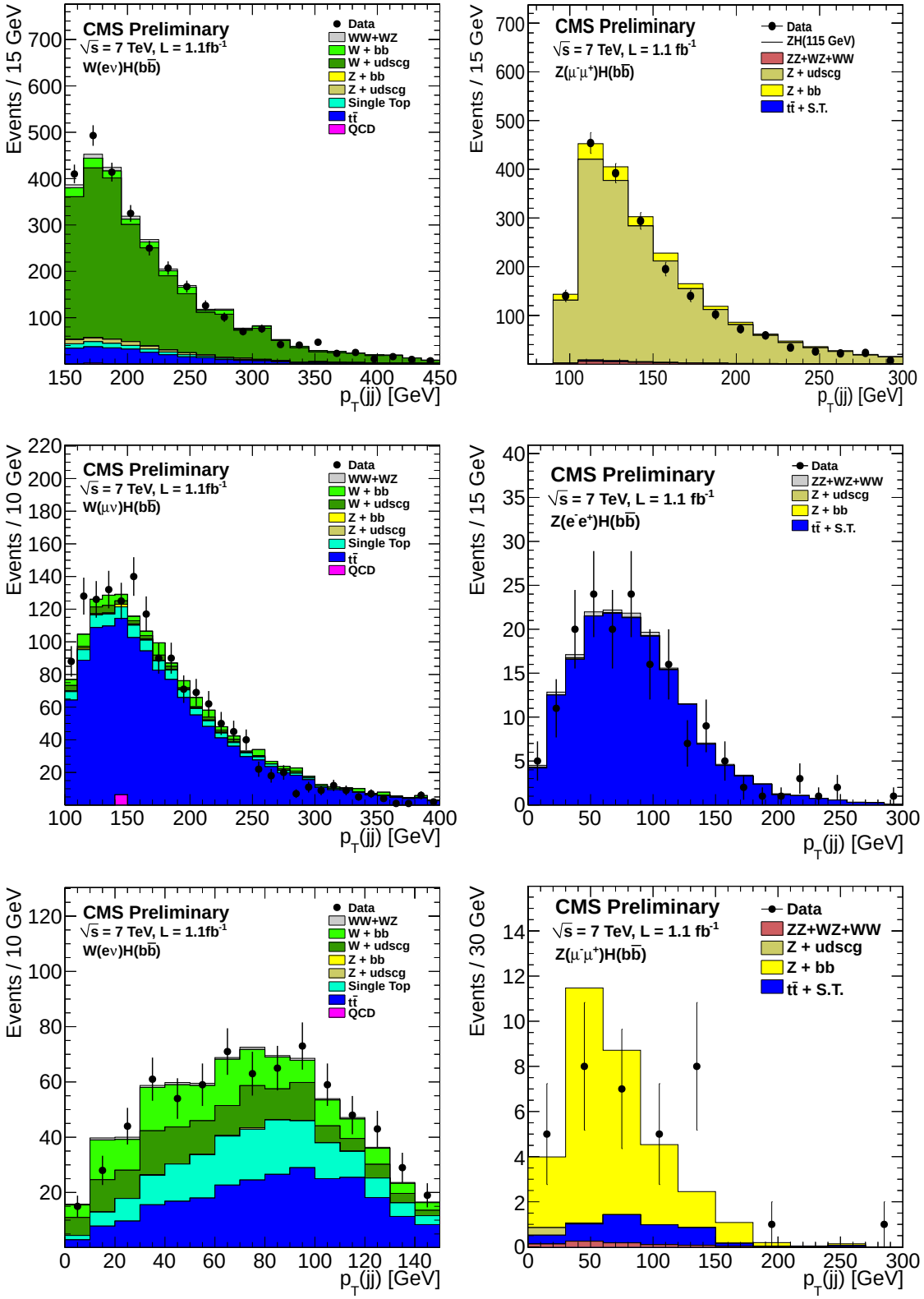

Figure 1: Distributions of dijet transverse momentum for events enhanced in production of V + udscg (top row), $t\bar{t}$ (middle row), and V$b\bar{b}$ (bottom row). Examples are shown for events reconstructed as W($e\nu$)H (top and bottom left), W($\mu\nu$)H (middle left), Z($\mu\mu$)H (top and bottom right), and Z(ee)H (middle right). Simulation is normalized to the data to facilitate the shape comparison.

Table 5: Z_{inv} Purity and scale factors (Data/MC) derived from background enriched control regions, as described in the text.

Control region	Purity	SF
$Z + udscg$	92.4%	0.97 ± 0.06
$W + udscg$	94.1%	0.92 ± 0.05
$Zb\bar{b}$	44.4%	1.00 ± 0.30
$t\bar{t}$	89.9%	0.91 ± 0.09

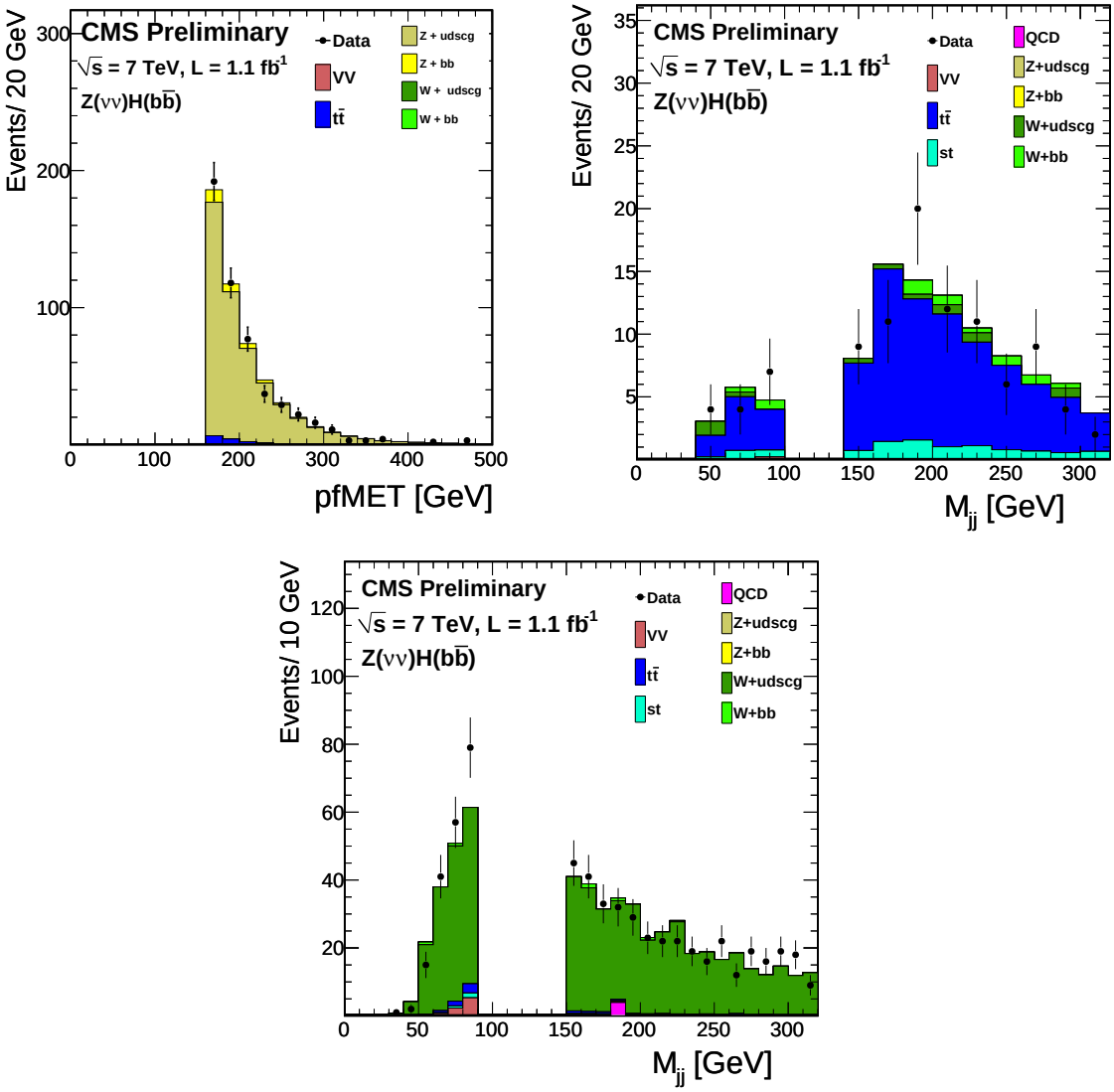

Figure 2: Examples of control regions for the $Z(\nu\nu)H$ analysis. Dijet p_T distribution from a $Z(\mu\mu)$+jets data sample, with removed muons, compared to simulated $Z(\nu\bar{\nu})$+jets events (top left). Distribution of dijet invariant mass for the $t\bar{t}$ (top right) and W+jets (bottom) control regions. The simulation has been normalized to the data.

6 Systematic Uncertainties

The primary physics result described in this note is an upper limit on the production of a standard model Higgs boson produced in association with a vector boson and decaying to a $b\bar{b}$ pair.

The following systematic uncertainties on the expected signal and background yields affect the upper limit. The values listed are an approximation of what is actually used in the limit calculation.

- **Luminosity**: The CMS luminosity uncertainty for this dataset was estimated to be 4.5%.
- **Lepton Efficiency**: muon and electron trigger, reconstruction, and identification efficiencies are determined in data using the standard tag-and-probe technique (TnP) with Z bosons. The systematic uncertainty is evaluated from the statistical uncertainties in the bin-by-bin efficiencies and scale factors as applied to signal Monte Carlo samples. The total uncertainty is $\sim 2\%$ per lepton.
- **MET+jets Trigger**: the parameters describing the trigger efficiency curve have been varied within their statistical uncertainties. An uncertainty of $+1.5, -3.2\%$ was estimated $Z(\nu\nu)H$.
- **Unclustered MET**: An uncertainty of 3% is assigned to the yields due to energy fluctuations not associated to jets.
- **Jet Energy Scale (JES)**: the jet energy scale was varied within one standard deviation based on p_T and η, and the efficiency of the analysis selection was recomputed to assess the systematic variation. An uncertainty of 1% was obtained.
- **Jet Energy Resolution (JER)**: the effect of uncertainty on the jet energy resolution was evaluated by scaling the measured resolution on a jet-by-jet basis. An uncertainty of $\sim 10\%$ was measured for all processes.
- **B-jet Tagging**: b-tagging data to simulation scale factors are applied consistently to jets in signal and background events. A systematic uncertainty of 10%, per b-tag, is assigned to all channels.
- **Signal cross section**: the total cross section has been calculated to next-to-next-to-leading order accuracy, and the total uncertainty is 4% [44, 45], including the effect of scale and PDF variations.
- **Theoretical H p_T Spectrum**: this analysis is performed in the boosted regime, and thus, potential differences in the p_T spectrum of the V and H between data and Monte Carlo generators could introduce systematic effects in the signal acceptance and efficiency estimates. Recently, two calculations have become available that estimate the NLO electroweak [46–48] and NNLO QCD [49] corrections to VH production in the boosted regime. The estimated effect from electroweak corrections for a boost of $\sim 150\,\text{GeV}$ are 5% for ZH and 10% for WH. For the QCD correction, the relevant comparison is NNLO vs. NLO, where an uncertainty of 10% for both ZH and WH is estimated.
- **Background Estimate**: a mix of data-driven methods, simulation, and theory uncertainties contribute to the total uncertainty on the background estimates, which are listed in Tables 6–15. Correlated (luminosity, b-tagging, JEC/JER, and TnP efficiencies) and uncorrelated uncertainties (statistical, control region, and cross section) are combined separately. An uncertainty of 30% is assumed for single top (approxi-

mately the uncertainty on the measured cross section) and diboson (assumed to have the same uncertainty as the signal). The other backgrounds are taken directly from data, with the associated uncertainties from the control regions.

- **Monte Carlo Statistics**: the finite size of the signal Monte Carlo signal samples contributes 4% across all channels, while the background statistical uncertainty can be large depending on the channel and the background source.

The total uncertainty on the signal prediction is taken to be 26% and 28% for ZH and WH production, respectively. Background uncertainties range from 12% to 20% depending on mode and mass point.

7 Results

The final predicted number of events in the signal regions of the BDT and $M(\mathrm{jj})$ analyses are determined with a mix of data-driven estimates based on the control regions described in Sec. 5, and expectations from simulation. This section summarizes all of the final signal and background estimates in both sets of analyses, including the systematic uncertainties summarized in the previous section, and the expected and observed upper limits using 1.1 fb^{-1} of integrated luminosity. The analyses were performed blind, in the sense that the analysis selection was decided and frozen before the signal region in each channel was investigated.

7.1 Signal and background estimates

Tables 6-10 summarize the expected signal and background yields, and the observed number of events, in the signal region for each channel for the $M(\mathrm{jj})$ analyses. Tables 11-15 summarize the expected signal and background yields, and the observed number of events, in the signal region for the `BDT` analyses. The BDT is retrained separately at each mass point. Single-top backgrounds are labeled "ST" in all tables. The QCD background contribution was found to be negligible in all channels and is not listed.

The final $M(\mathrm{jj})$ distributions and the final BDT distributions are shown in Fig. 3 and in Fig. 4, respectively. The data is overlaid with the predicted background normalization.

Table 6: Predicted backgrounds including the statistical uncertainty and the systematic uncertainty from the control region and b-tag scale factors, signal yields with total uncertainty, and the observed number of events for each mass point in the $\mathrm{W}(\mu\nu)\mathrm{H}$ $M(\mathrm{jj})$ analysis.

Process	110 GeV	115 GeV	120 GeV	125 GeV	130 GeV	135 GeV
$\mathrm{W}+\mathrm{udscg}$	0.105 ± 0.050	0.081 ± 0.038	0.068 ± 0.032	0.045 ± 0.021	0.061 ± 0.029	0.096 ± 0.045
$\mathrm{Wb\bar{b}}$	0.876 ± 0.233	0.829 ± 0.221	0.796 ± 0.212	0.703 ± 0.187	0.572 ± 0.152	0.516 ± 0.137
Z+jets	0.178 ± 0.127	0.184 ± 0.131	0.006 ± 0.004	0.252 ± 0.180	0.252 ± 0.180	0.252 ± 0.180
$\mathrm{t\bar{t}}$	1.17 ± 0.303	1.109 ± 0.287	1.207 ± 0.313	1.232 ± 0.319	1.107 ± 0.287	1.209 ± 0.313
ST	0.254 ± 0.111	0.24 ± 0.105	0.25 ± 0.109	0.271 ± 0.118	0.285 ± 0.124	0.223 ± 0.097
VV	0.244 ± 0.102	0.153 ± 0.064	0.039 ± 0.016	0.021 ± 0.009	0.017 ± 0.007	0.009 ± 0.004
B_{exp}	2.827 ± 0.482	2.596 ± 0.449	2.366 ± 0.434	2.524 ± 0.461	2.294 ± 0.421	2.305 ± 0.428
WH	0.378 ± 0.106	0.354 ± 0.099	0.296 ± 0.083	0.236 ± 0.066	0.187 ± 0.052	0.143 ± 0.040
ZH	0.006 ± 0.002	0.006 ± 0.002	0.006 ± 0.002	0.005 ± 0.001	0.003 ± 0.001	0.002 ± 0.001
N_{obs}	2	4	4	4	3	3

Table 7: Predicted backgrounds including the statistical uncertainty and the systematic uncertainty from the control region and b-tag scale factors, signal yields with total uncertainty, and the observed number of events for each mass point in the $W(e\nu)H$ $M(jj)$ analysis.

Process	110 GeV	115 GeV	120 GeV	125 GeV	130 GeV	135 GeV
$W + udscg$	0.036 ± 0.015	0.01 ± 0.004	0.011 ± 0.004	0.013 ± 0.005	0.012 ± 0.005	0.027 ± 0.011
$Wb\bar{b}$	0.442 ± 0.120	0.344 ± 0.093	0.375 ± 0.102	0.370 ± 0.100	0.32 ± 0.087	0.265 ± 0.072
Z+jets	0.204 ± 0.146	0.204 ± 0.146	0	0	0	0
$t\bar{t}$	0.767 ± 0.193	0.543 ± 0.136	0.543 ± 0.136	0.503 ± 0.126	0.568 ± 0.143	0.403 ± 0.101
ST	0.076 ± 0.030	0.122 ± 0.049	0.181 ± 0.072	0.283 ± 0.113	0.32 ± 0.128	0.385 ± 0.154
VV	0.134 ± 0.053	0.065 ± 0.026	0.045 ± 0.018	0.042 ± 0.017	0.033 ± 0.013	0.029 ± 0.012
B_{exp}	1.66 ± 0.299	1.288 ± 0.242	1.155 ± 0.206	1.211 ± 0.217	1.253 ± 0.228	1.109 ± 0.209
WH	0.263 ± 0.074	0.296 ± 0.083	0.203 ± 0.057	0.201 ± 0.056	0.142 ± 0.040	0.123 ± 0.034
ZH	0.004 ± 0.001	0.002 ± 0.001	0.003 ± 0.001	0.002 ± 0.001	0.002 ± 0.001	0.001 ± 0.001
N_{obs}	4	4	1	1	0	0

Table 8: Predicted backgrounds including the statistical uncertainty and the systematic uncertainty from the control region and b-tag scale factors, signal yields with total uncertainty, and the observed number of events for each mass point in the $Z(\mu\mu)H$ $M(jj)$ analysis.

Process	110 GeV	115 GeV	120 GeV	125 GeV	130 GeV	135 GeV
$Z + udscg$	0.110 ± 0.064	0.110 ± 0.065	0.110 ± 0.065	0.110 ± 0.065	0.150 ± 0.069	0.110 ± 0.065
$Zb\bar{b}$	1.930 ± 0.337	2.050 ± 0.396	1.650 ± 0.373	1.740 ± 0.378	1.660 ± 0.375	1.600 ± 0.361
$t\bar{t}$ + ST	0.030 ± 0.031	0.090 ± 0.036	0.140 ± 0.044	0.140 ± 0.044	0.190 ± 0.053	0.190 ± 0.127
VV	0.260 ± 0.100	0.160 ± 0.064	0.070 ± 0.033	0.030 ± 0.023	0.020 ± 0.021	0.010 ± 0.011
B_{exp}	2.330 ± 0.363	2.410 ± 0.358	1.970 ± 0.348	2.020 ± 0.348	2.020 ± 0.351	1.910 ± 0.356
S	0.218 ± 0.057	0.195 ± 0.051	0.152 ± 0.040	0.128 ± 0.033	0.102 ± 0.027	0.077 ± 0.020
N_{obs}	3	3	3	3	2	3

Table 9: Predicted backgrounds including the statistical uncertainty and the systematic uncertainty from the control region and b-tag scale factors, signal yields with total uncertainty, and the observed number of events for each mass point in the $Z(ee)H$ $M(jj)$ analysis.

Process	110 GeV	115 GeV	120 GeV	125 GeV	130 GeV	135 GeV
$Z + udscg$	0.013 ± 0.006	0.006 ± 0.003	0.004 ± 0.003	0.007 ± 0.004	0.024 ± 0.012	0.028 ± 0.013
$Zb\bar{b}$	1.327 ± 0.173	1.545 ± 0.254	1.300 ± 0.214	1.472 ± 0.242	1.581 ± 0.250	1.372 ± 0.217
$t\bar{t}$	0.105 ± 0.052	0.133 ± 0.073	0.090 ± 0.050	0.090 ± 0.050	0.070 ± 0.044	0.070 ± 0.044
ST	0.009 ± 0.007	0.009 ± 0.007	0.028 ± 0.022	0.019 ± 0.020	0.019 ± 0.020	0.019 ± 0.020
VV	0.236 ± 0.091	0.189 ± 0.074	0.104 ± 0.041	0.066 ± 0.027	0.037 ± 0.016	0.024 ± 0.011
B_{exp}	1.690 ± 0.209	1.883 ± 0.232	1.526 ± 0.186	1.655 ± 0.203	1.731 ± 0.201	1.513 ± 0.177
S	0.211 ± 0.055	0.193 ± 0.050	0.148 ± 0.038	0.136 ± 0.035	0.102 ± 0.027	0.081 ± 0.021
N_{obs}	1	2	2	2	3	4

Table 10: Predicted backgrounds including the statistical uncertainty and the systematic uncertainty from the control region and b-tag scale factors, signal yields with total uncertainty, and the observed number of events for each mass point in the $Z(\nu\nu)H$ $M(jj)$ analysis.

Process	110 GeV	115 GeV	120 GeV	125 GeV	130 GeV	135 GeV
$W + udscg$	0.024 ± 0.007	0.023 ± 0.007	0.022 ± 0.007	0.019 ± 0.006	0.014 ± 0.004	0.012 ± 0.004
$Wb\bar{b}$+ $t\bar{t}$	2.030 ± 0.609	1.780 ± 0.534	2.050 ± 0.615	2.360 ± 0.708	2.420 ± 0.726	2.110 ± 0.633
$Z + udscg$	0.180 ± 0.039	0.180 ± 0.039	0.140 ± 0.030	0.130 ± 0.028	0.120 ± 0.026	0.130 ± 0.028
$Zb\bar{b}$	1.970 ± 0.603	1.890 ± 0.578	1.790 ± 0.548	1.710 ± 0.523	1.780 ± 0.545	1.810 ± 0.554
ST	0.460 ± 0.174	0.460 ± 0.174	0.410 ± 0.155	0.410 ± 0.155	0.460 ± 0.174	0.400 ± 0.152
VV	0.770 ± 0.292	0.460 ± 0.174	0.410 ± 0.155	0.110 ± 0.042	0.080 ± 0.030	0.070 ± 0.027
B_{exp}	5.434 ± 1.069	4.793 ± 0.938	4.822 ± 0.958	4.739 ± 0.969	4.874 ± 0.998	4.532 ± 0.918
S	0.669 ± 0.174	0.593 ± 0.154	0.417 ± 0.108	0.442 ± 0.115	0.326 ± 0.085	0.245 ± 0.064
N_{obs}	6	5	5	5	6	5

Table 11: Predicted backgrounds including the statistical uncertainty and the systematic uncertainty from the control region and b-tag scale factors, signal yields with total uncertainty, and the observed number of events for each mass point in the $W(\mu\nu)H$ BDT analysis.

Process	110 GeV	115 GeV	120 GeV	125 GeV	130 GeV	135 GeV
$W + udscg$	0.661 ± 0.191	0.667 ± 0.192	0.546 ± 0.157	0.628 ± 0.181	0.697 ± 0.201	0.446 ± 0.129
$Wb\bar{b}$	2.460 ± 0.644	2.035 ± 0.533	2.083 ± 0.545	2.698 ± 0.706	2.086 ± 0.546	2.450 ± 0.641
Z+jets	0	0.006 ± 0.006	0.190 ± 0.190	0.367 ± 0.368	0.245 ± 0.246	0.190 ± 0.190
$t\bar{t}$	1.667 ± 0.432	1.173 ± 0.304	1.362 ± 0.353	2.239 ± 0.580	2.262 ± 0.586	2.196 ± 0.569
ST	0.608 ± 0.243	0.653 ± 0.261	0.673 ± 0.269	0.956 ± 0.382	1.007 ± 0.402	1.055 ± 0.421
VV	0.496 ± 0.195	0.355 ± 0.140	0.345 ± 0.136	0.283 ± 0.111	0.216 ± 0.085	0.159 ± 0.063
B_{exp}	5.892 ± 0.980	4.889 ± 0.806	5.199 ± 0.857	7.171 ± 1.206	6.513 ± 1.074	6.496 ± 1.100
WH	0.619 ± 0.173	0.587 ± 0.164	0.499 ± 0.140	0.416 ± 0.116	0.383 ± 0.107	0.281 ± 0.079
ZH	0.015 ± 0.004	0.011 ± 0.003	0.012 ± 0.003	0.011 ± 0.003	0.007 ± 0.002	0.006 ± 0.002
N_{obs}	9	7	6	5	11	11

Table 12: Predicted backgrounds including the statistical uncertainty and the systematic uncertainty from the control region and b-tag scale factors, signal yields with total uncertainty, and the observed number of events for each mass point in the $W(e\nu)H$ BDT analysis.

Process	110 GeV	115 GeV	120 GeV	125 GeV	130 GeV	135 GeV
$W + udscg$	0.148 ± 0.060	0.155 ± 0.063	0.241 ± 0.097	0.300 ± 0.121	0.342 ± 0.138	0.220 ± 0.089
$Wb\bar{b}$	1.112 ± 0.302	1.378 ± 0.374	1.015 ± 0.276	1.390 ± 0.377	0.962 ± 0.261	1.063 ± 0.289
Z+jets	0	0.198 ± 0.141	0.198 ± 0.141	0.238 ± 0.170	0.198 ± 0.141	0.198 ± 0.141
$t\bar{t}$	0.790 ± 0.198	1.254 ± 0.315	2.037 ± 0.511	2.008 ± 0.504	1.996 ± 0.501	2.533 ± 0.636
ST	0.381 ± 0.152	0.653 ± 0.261	0.658 ± 0.263	0.920 ± 0.367	1.081 ± 0.431	1.268 ± 0.506
VV	0.343 ± 0.137	0.292 ± 0.117	0.232 ± 0.093	0.201 ± 0.080	0.151 ± 0.060	0.138 ± 0.055
B_{exp}	2.774 ± 0.476	3.930 ± 0.658	4.381 ± 0.742	5.057 ± 0.849	4.730 ± 0.811	5.420 ± 0.954
WH	0.441 ± 0.123	0.477 ± 0.134	0.393 ± 0.110	0.344 ± 0.096	0.274 ± 0.077	0.233 ± 0.065
ZH	0.005 ± 0.001	0.004 ± 0.001	0.007 ± 0.002	0.006 ± 0.002	0.004 ± 0.001	0.004 ± 0.001
N_{obs}	6	9	7	9	5	5

Table 13: Predicted backgrounds including the statistical uncertainty and the systematic uncertainty from the control region and b-tag scale factors, signal yields with total uncertainty, and the observed number of events for each mass point in the Z($\mu\mu$)H BDT analysis.

Process	110 GeV	115 GeV	120 GeV	125 GeV	130 GeV	135 GeV
Z + udscg	2.023 ± 0.575	1.225 ± 0.490	1.002 ± 0.426	0.696 ± 0.395	0.585 ± 0.386	0.341 ± 0.225
Zb$\bar{\text{b}}$	4.470 ± 0.621	2.858 ± 0.645	3.435 ± 0.776	2.772 ± 0.746	2.386 ± 0.707	4.245 ± 0.854
t$\bar{\text{t}}$	0.409 ± 0.225	0.296 ± 0.218	0.460 ± 0.278	0.601 ± 0.293	0.684 ± 0.304	0.873 ± 0.410
ST	0.060 ± 0.064	0.060 ± 0.064	0.060 ± 0.064	0	0.060 ± 0.064	0.060 ± 0.064
VV	0.636 ± 0.243	0.334 ± 0.130	0.507 ± 0.197	0.344 ± 0.141	0.089 ± 0.052	0.161 ± 0.065
B_{exp}	7.598 ± 1.018	4.773 ± 0.841	5.464 ± 0.938	4.413 ± 0.896	3.804 ± 0.855	5.680 ± 0.902
S	0.440 ± 0.114	0.328 ± 0.085	0.295 ± 0.077	0.244 ± 0.063	0.164 ± 0.043	0.148 ± 0.038
N_{obs}	9	4	7	4	4	7

Table 14: Predicted backgrounds including the statistical uncertainty and the systematic uncertainty from the control region and b-tag scale factors, signal yields with total uncertainty, and the observed number of events for each mass point in the Z(ee)H BDT analysis.

Process	110 GeV	115 GeV	120 GeV	125 GeV	130 GeV	135 GeV
Z + udscg	0.459 ± 0.174	0.077 ± 0.036	0.120 ± 0.056	0.140 ± 0.058	0.290 ± 0.116	0.310 ± 0.116
Zb$\bar{\text{b}}$	0.699 ± 0.129	0.904 ± 0.189	1.117 ± 0.216	1.040 ± 0.193	1.441 ± 0.268	1.535 ± 0.274
t$\bar{\text{t}}$	0.223 ± 0.121	0.179 ± 0.133	0.455 ± 0.284	0	0.286 ± 0.213	0.170 ± 0.127
ST	0.002 ± 0.001	0	0.018 ± 0.019	0	0.002 ± 0.002	0.007 ± 0.008
VV	0.230 ± 0.091	0.195 ± 0.078	0.177 ± 0.071	0.159 ± 0.065	0.124 ± 0.051	0.115 ± 0.048
B_{exp}	1.614 ± 0.301	1.354 ± 0.240	1.887 ± 0.367	1.339 ± 0.189	2.142 ± 0.351	2.136 ± 0.302
S	0.209 ± 0.054	0.183 ± 0.048	0.161 ± 0.042	0.130 ± 0.034	0.121 ± 0.031	0.102 ± 0.027
N_{obs}	1	2	2	2	3	3

Table 15: Predicted backgrounds including the statistical uncertainty and the systematic uncertainty from the control region and b-tag scale factors, signal yields with total uncertainty, and the observed number of events for each mass point in the Z($\nu\nu$)H BDT analysis.

Process	110 GeV	115 GeV	120 GeV	125 GeV	130 GeV	135 GeV
Wb$\bar{\text{b}}$+ t$\bar{\text{t}}$	0.656 ± 0.197	0.656 ± 0.197	0.525 ± 0.158	0.787 ± 0.236	0.263 ± 0.079	0.394 ± 0.118
Z + udscg	0.581 ± 0.126	0.113 ± 0.025	0.174 ± 0.038	0.222 ± 0.048	0.281 ± 0.061	0.341 ± 0.074
Zb$\bar{\text{b}}$	1.256 ± 0.384	1.108 ± 0.339	1.182 ± 0.362	0.936 ± 0.286	1.207 ± 0.369	1.034 ± 0.316
ST	0.452 ± 0.171	0.453 ± 0.172	0.432 ± 0.164	0.411 ± 0.156	0.543 ± 0.206	0.853 ± 0.323
VV	0.843 ± 0.319	0.571 ± 0.216	0.252 ± 0.095	0.291 ± 0.110	0.063 ± 0.024	0.351 ± 0.133
B_{exp}	3.992 ± 0.730	2.901 ± 0.572	2.565 ± 0.500	2.648 ± 0.510	2.357 ± 0.475	2.973 ± 0.596
S	0.642 ± 0.167	0.548 ± 0.142	0.352 ± 0.092	0.317 ± 0.082	0.259 ± 0.067	0.216 ± 0.056
N_{obs}	2	1	1	5	2	3

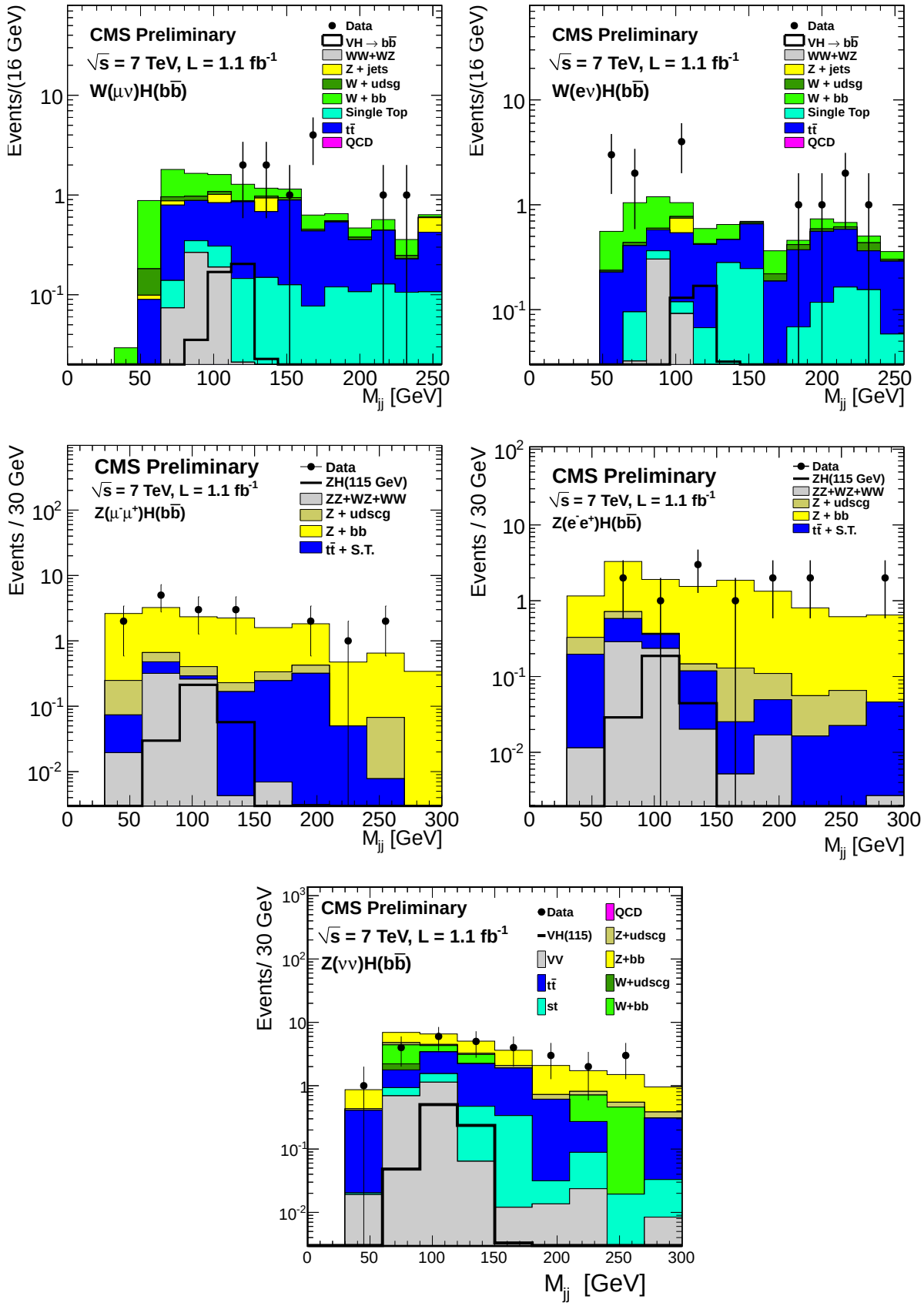

Figure 3: Distributions of dijet invariant mass after all $M(\mathrm{jj})$ selection criteria have been applied in (clockwise from top left to bottom right: $\mathrm{W}(\mu\nu)\mathrm{H}$, $\mathrm{W}(\mathrm{e}\nu)\mathrm{H}$, $\mathrm{Z}(\mu\mu)\mathrm{H}$, $\mathrm{Z}(\mathrm{ee})\mathrm{H}$, $\mathrm{Z}(\nu\nu)\mathrm{H}$.

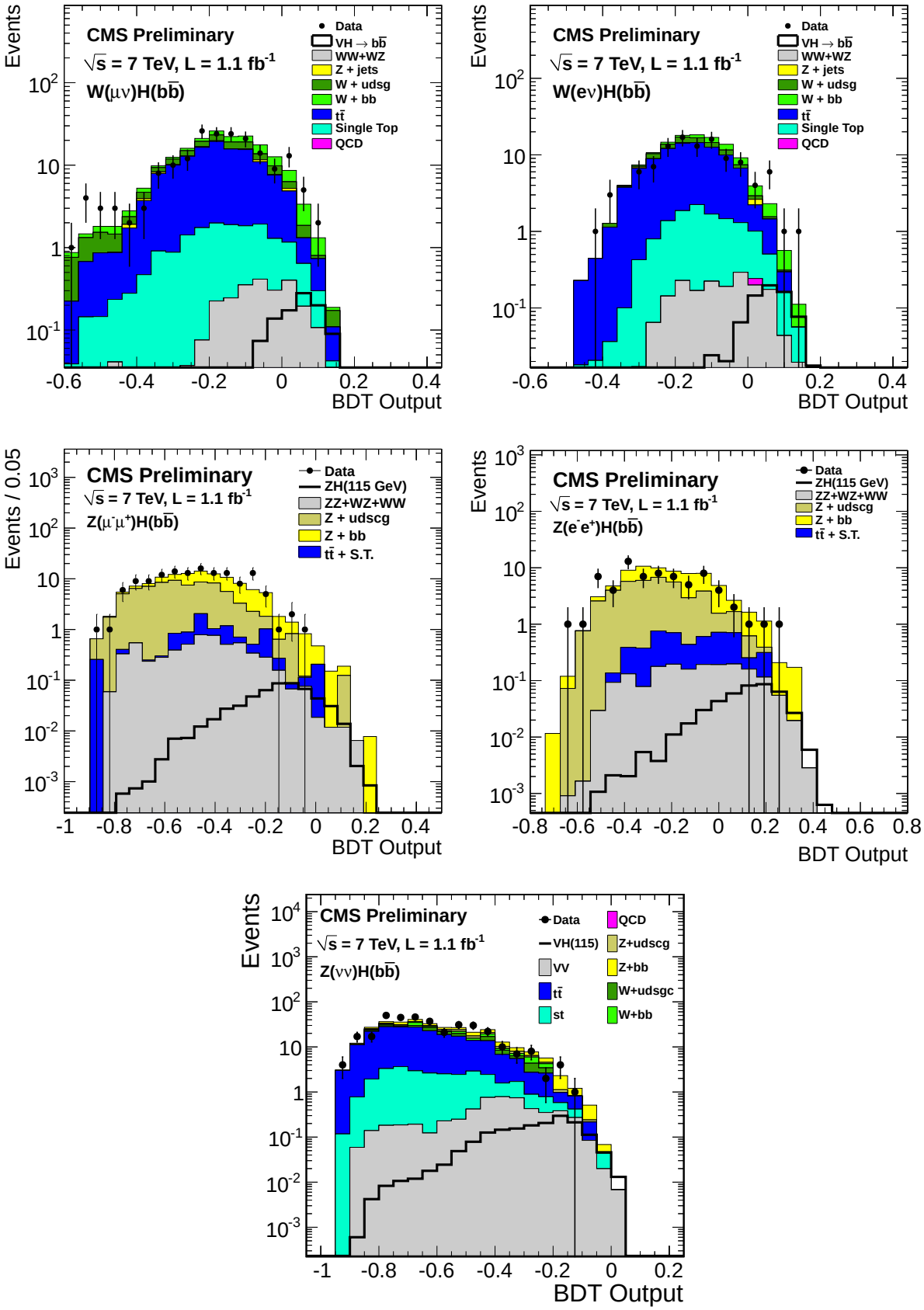

Figure 4: Distributions of BDT output for data (points with errors) and all backgrounds: W($\mu\nu$)H (top left), W(eν)H (top right), Z($\mu\mu$)H (middle left), Z(ee)H (middle right) and Z($\nu\nu$)H)bottom.

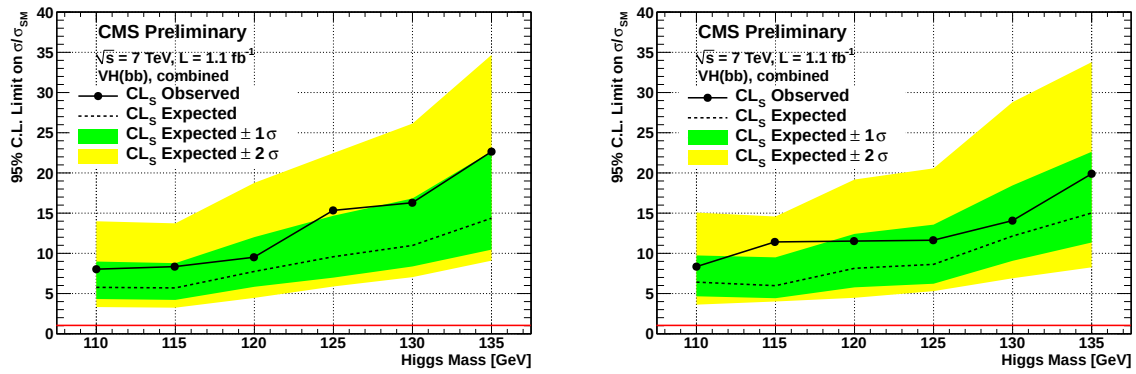

Figure 5: Expected and observed 95% C.L. combined upper limits on the ratio of VHbb production for the BDT (left) and $M(\mathrm{jj})$ (right) analyses. The median expected limit and the 1- and 2-σ bands are obtained with the LHC CLs method as implemented in LandS, as are the observed limits at each mass point.

Table 16: Expected and observed 95% CL upper limits on the production of a SM Higgs boson in association with W and Z bosons and decaying to b quarks relative to the expected cross section. Limits are listed separately for the BDT and $M(\mathrm{jj})$ analyses.

M_{H}(GeV)	BDT Expected	BDT Observed	$M(\mathrm{jj})$ Expected	$M(\mathrm{jj})$ Observed
110	5.8	8.0	6.4	8.2
115	5.7	8.3	6.0	11.3
120	7.7	9.5	8.1	11.4
125	9.6	15.3	8.6	11.6
130	11.0	16.3	12.1	14.0
135	14.4	22.5	15.0	19.9

7.2 Upper limits

Preliminary 95% C.L. upper limits on the Higgs production cross section in the VH mode with $\mathrm{H} \to \mathrm{b\bar{b}}$ were obtained from both the BDT and $M(\mathrm{jj})$ analyses for a dataset corresponding to an integrated luminosity of 1.1 fb^{-1}. The limits were calculated using the LandS code [50]. The results were also checked with the standard RooStats configuration [51], and found to be consistent. For the expected and observed limits, and the 1- and 2-σ bands, the CLs method currently recommended by the LHC Higgs Combination Group was employed [52]. Signal and background uncertainties, as described in the previous sections, were included as nuisance parameters in the calculation, with appropriate correlations taken into account.

The results of the five BDT analyses are combined to produce limits on Higgs production in the $\mathrm{b\bar{b}}$ channel for the assumed masses: $110 - 135$ GeV. The identical procedure was applied to the results of the $M(\mathrm{jj})$ analysis. Table 16 summarizes the resulting, expected and observed, upper 95% C.L. cross section limits, with respect to the standard model cross section, for each of the mass points for the BDT and $M(\mathrm{jj})$ analyses. The results are displayed separately in Fig. 5. The primary result is the one from the BDT analysis.

8 Conclusions

This note reports the first cross section upper limits from the CMS experiment for standard model Higgs production in association with vector bosons and decaying to $b\bar{b}$ pairs. A data sample corresponding to an integrated luminosity of 1.1 fb^{-1} has been analyzed in these channels: W($\mu\nu$)H, W(eν)H, Z($\mu\mu$)H, Z(ee)H, Z($\nu\nu$)H, and 95% C.L. upper limits were derived in a Higgs mass range from $110 - 135$ GeV using the results from the BDT analyses. At 115 GeV the expected (observed) upper limit is 5.7 (8.3) times the standard model cross section. These results can be directly compared to a recent analysis from the ATLAS experiment [53].

References

[1] F. Englert and R. Brout, "Broken symmetries and the masses of gauge bosons", *Phys. Rev. Lett.* **13** (1964) 321. doi:10.1103/PhysRevLett.13.321.

[2] P. W. Higgs, "Broken symmetry and the mass of gauge vector mesons", *Phys. Rev. Lett.* **13** (1964) 508. doi:10.1103/PhysRevLett.13.508.

[3] G. Guralnik, C. Hagen, and T. Kibble, "Global Conservation Laws and Massless Particles", *Phys.Rev.Lett.* **13** (1964) 585–587. doi:10.1103/PhysRevLett.13.585.

[4] ALEPH, CDF, D0, DELPHI, L3, OPAL, SLD Collaborations, the LEP Electroweak Working Group, the Tevatron Electroweak Working Group, and the SLD Electroweak and Heavy Flavour Groups, "Precision electroweak measurements and constraints on the Standard Model",. arXiv:1012.2367.

[5] ALEPH, DELPHI, L3, OPAL Collaborations, and The LEP Working Group for Higgs Boson Searches, "Search for the Standard Model Higgs boson at LEP", *Phys. Lett.* **B565** (2003) 61. doi:10.1016/S0370-2693(03)00614-2.

[6] T. CDF, D. Collaborations, t. T. N. Phenomena et al., "Combined CDF and D0 Upper Limits on Standard Model Higgs Boson Production with up to 8.6 fb-1 of Data", arXiv:1107.5518.

[7] CMS Collaboration, "Search for Higgs Boson Decays to Two W Bosons in the Fully Leptonic Final State at $\sqrt{s} = 7$ TeV with 2011 data of CMS detector", *CMS Physics Analysis Summary,* **HIG-11-003** (2011).

[8] CMS Collaboration, "Search for a Standard Model Higgs boson produced in the decay channel H$\to$ZZ$^{(*)} \to 4\ell$", *CMS Physics Analysis Summary,* **HIG-11-004** (2011).

[9] CMS Collaboration, "Search for a Standard Model Higgs boson using the $H \to ZZ^{(*)} \to 2\ell 2\nu$ decay mode in pp-collisions at $\sqrt{s} = 7$ TeV", *CMS Physics Analysis Summary,* **HIG-11-005** (2011).

[10] CMS Collaboration, "Search for a SM Higgs or BSM Boson H$\to$ZZ$\to$ $(\ell^+\ell^-)(q\bar{q})$", *CMS Physics Analysis Summary,* **HIG-11-006** (2011).

[11] CMS Collaboration, "Search for Neutral Higgs Bosons Decaying to Tau Pairs in pp Collisions at $\sqrt{s} = 7$ TeV", *CMS Physics Analysis Summary,* **HIG-11-009** (2011).

[12] CMS Collaboration, "Search for a Higgs boson decaying into two photons in proton-proton collisions recorded by the CMS detector at the LHC", *CMS Physics Analysis Summary,* **HIG-11-010** (2011).

[13] ATLAS Collaboration, "Combination of the Searches for the Higgs Boson in 1 fb^{-1} of Data Taken with the ATLAS Detector at 7 TeV Center-of-Mass Energy", *ATLAS Note,* **ATLAS-CONF-2011-112** (2011).

[14] S. Dawson, "Radiative corrections to Higgs boson production", *Nucl. Phys.* **B359** (1991) 283–300. doi:10.1016/0550-3213(91)90061-2.

[15] M. Spira, A. Djouadi, D. Graudenz et al., "Higgs boson production at the LHC", *Nucl. Phys.* **B453** (1995) 17–82, arXiv:hep-ph/9504378. doi:10.1016/0550-3213(95)00379-7.

[16] R. V. Harlander and W. B. Kilgore, "Next-to-next-to-leading order Higgs production at hadron colliders", *Phys. Rev. Lett.* **88** (2002) 201801, arXiv:hep-ph/0201206. doi:10.1103/PhysRevLett.88.201801.

[17] C. Anastasiou and K. Melnikov, "Higgs boson production at hadron colliders in NNLO QCD", *Nucl. Phys.* **B646** (2002) 220–256, arXiv:hep-ph/0207004. doi:10.1016/S0550-3213(02)00837-4.

[18] V. Ravindran, J. Smith, and W. L. van Neerven, "NNLO corrections to the total cross section for Higgs boson production in hadron hadron collisions", *Nucl. Phys.* **B665** (2003) 325–366, arXiv:hep-ph/0302135. doi:10.1016/S0550-3213(03)00457-7.

[19] S. Catani, D. de Florian, M. Grazzini et al., "Soft-gluon resummation for Higgs boson production at hadron colliders", *JHEP* **07** (2003) 028, arXiv:hep-ph/0306211.

[20] S. Actis, G. Passarino, C. Sturm et al., "NLO Electroweak Corrections to Higgs Boson Production at Hadron Colliders", *Phys. Lett.* **B670** (2008) 12–17, arXiv:0809.1301. doi:10.1016/j.physletb.2008.10.018.

[21] M. Ciccolini, A. Denner, and S. Dittmaier, "Strong and electroweak corrections to the production of Higgs + 2-jets via weak interactions at the LHC", *Phys. Rev. Lett.* **99** (2007) 161803, arXiv:0707.0381. doi:10.1103/PhysRevLett.99.161803.

[22] M. Ciccolini, A. Denner, and S. Dittmaier, "Electroweak and QCD corrections to Higgs production via vector-boson fusion at the LHC", *Phys. Rev.* **D77** (2008) 013002, arXiv:0710.4749. doi:10.1103/PhysRevD.77.013002.

[23] T. Figy, C. Oleari, and D. Zeppenfeld, "Next-to-leading order jet distributions for Higgs boson production via weak-boson fusion", *Phys. Rev.* **D68** (2003) 073005, arXiv:hep-ph/0306109. doi:10.1103/PhysRevD.68.073005.

[24] K. Arnold et al., "VBFNLO: A parton level Monte Carlo for processes with electroweak bosons", *Comput. Phys. Commun.* **180** (2009) 1661–1670, arXiv:0811.4559. doi:10.1016/j.cpc.2009.03.006.

[25] P. Bolzoni, F. Maltoni, S.-O. Moch et al., "Higgs production via vector-boson fusion at NNLO in QCD", *Phys. Rev. Lett.* **105** (2010) 011801, arXiv:1003.4451. doi:10.1103/PhysRevLett.105.011801.

[26] C. Anastasiou, R. Boughezal, and F. Petriello, "Mixed QCD-electroweak corrections to Higgs boson production in gluon fusion", *JHEP* **04** (2009) 003, arXiv:0811.3458. doi:10.1088/1126-6708/2009/04/003.

[27] D. de Florian and M. Grazzini, "Higgs production through gluon fusion: updated cross sections at the Tevatron and the LHC", *Phys. Lett.* **B674** (2009) 291–294, arXiv:0901.2427. doi:10.1016/j.physletb.2009.03.033.

[28] A. Djouadi, J. Kalinowski, M. Muhlleitner et al., "An update of the program HDECAY", in *The Les Houches 2009 workshop on TeV colliders: The tools and Monte Carlo working group summary report*. 2010. arXiv:1003.1643.

[29] LHC Higgs Cross Section Working Group, S. Dittmaier, C. Mariotti et al., "Handbook of LHC Higgs Cross Sections: 1. Inclusive Observables", *CERN-2011-002* (CERN, Geneva, 2011) arXiv:1101.0593.

[30] CMS Collaboration, "The CMS experiment at the CERN LHC", *JINST* **3** (2008) S08004. doi:10.1088/1748-0221/3/08/S08004.

[31] S. Agostinelli et al., "Geant 4 A Simulation Toolkit", *Nucl. Inst. Meth. A* **506** (2003) 250.

[32] S. Frixione, P. Nason, and C. Oleari, "Matching NLO QCD computations with Parton Shower simulations: the POWHEG method", *JHEP* **11** (2007) 070, arXiv:0709.2092.

[33] G. Corcella et al., "HERWIG 6.5: an event generator for Hadron Emission Reactions With Interfering Gluons (including supersymmetric processes)", *JHEP* **01** (2001) 010, arXiv:hep-ph/0011363.

[34] T. Sjostrand, S. Mrenna, and P. Skands, "PYTHIA 6.4 physics and manual", *JHEP* **05** (2007).

[35] F. Maltoni and T. Stelzer, "MadEvent: Automatic event generation with MadGraph", *JHEP 02* (2003) arXiv:0208156.

[36] CMS Collaboration, "Jet Performance in pp Collisions at $\sqrt{s}$=7 TeV", *CMS Physics Analysis Summary* **CMS-PAS-JME-10-003** (2010).

[37] M. Cacciari, G. P. Salam, and G. Soyez, "The anti-k_t jet clustering algorithm", *JHEP* **04** (2008) 063, arXiv:0802.1189.

[38] CMS Collaboration, "Jet Energy Calibration with Photon+Jet Events", *PAS JME-09-004* (2009).

[39] CMS Collaboration, "Electron reconstruction and identication at $\sqrt{s}$ = 7 TeV", *CMS Physics Analysis Summary* **CMS-PAS-EGM-10-004** (2010).

[40] CMS Collaboration, "Performance of muon identification in 2010 data", *CMS Physics Analysis Summary* **CMS-PAS-MUO-10-004** (2010).

[41] CMS Collaboration, "Algorithms for b jet identification in CMS", *CMS Physics Analysis Summary* **BTV-09-001** (2009).

[42] CMS Collaboration, "Performance of b-jet identification in CMS", *CMS Physics Analysis Summary* **BTV-11-001** (2011).

[43] A. Hoecker et al., "TMVA - toolkit for multivariate data analysis", arXiv:0703039.

[44] LHC Higgs Cross Section Working Group, S. Dittmaier, C. Mariotti et al., "Handbook of LHC Higgs Cross Sections: Inclusive Observables", arXiv:1101.0593.

[45] O. Brein, A. Djouadi, and R. Harlander, "NNLO QCD corrections to the Higgs-strahlung processes at hadron colliders", *Phys. Lett.* **B579** (2004) 149–156, arXiv:hep-ph/0307206. doi:10.1016/j.physletb.2003.10.112.

[46] M. Ciccolini, A. Denner, and S. Dittmaier, "Strong and electroweak corrections to the production of Higgs+2jets via weak interactions at the LHC", *Phys. Rev. Lett.* **99** (2007) 161803, arXiv:0707.0381. doi:10.1103/PhysRevLett.99.161803.

[47] M. Ciccolini, A. Denner, and S. Dittmaier, "Electroweak and QCD corrections to Higgs production via vector-boson fusion at the LHC", *Phys. Rev.* **D77** (2008) 013002, arXiv:0710.4749. doi:10.1103/PhysRevD.77.013002.

[48] Dittmaier, S., "NLO QCD and EWK corrections to Higgs-strahlung off W/Z bosons at Tevatron and the LHC with HAWK", *parallel session talk,* **EPS 2011, Grenoble, France,** (2011).

[49] G. Ferrera, M. Grazzini, and F. Tramontano, "Associated WH production at hadron colliders: a fully exclusive QCD calculation at NNLO", arXiv:1107.1164.* Temporary entry *.

[50] Chen, M. and Korytov, A., "Limits and Signifcance". https://mschen.web.cern.ch/mschen/LandS/.

[51] L. Moneta, K. Belasco, K. Cranmer et al., "The RooStats Project", in *13th International Workshop on Advanced Computing and Analysis Techniques in Physics Research (ACAT2010)*. SISSA, 2010. arXiv:1009.1003. PoS(ACAT2010)057.

[52] CMS Collaboration, "Search for standard model Higgs boson in pp collisions at $\sqrt{s} = 7$ TeV", *CMS Physics Analysis Summary,* **HIG-11-011** (2011).

[53] ATLAS Collaboration, "Search for the Standard Model Higgs boson produced in association with a vector boson and decaying to a b-quark pair with the ATLAS detector at the LHC", *ATLAS Note,* **ATLAS-CONF-2011-103** (2011).